Draft version May 8, 2020
Typeset using LaTeX **twocolumn** style in AASTeX63

Why We Should Kerr About the Dark Secrets of Relativistic Accretion Disks in Athena++

E. C. Rohr[1]
et al.
(Athena++)

[1]*Department of Astronomy, University of Virginia*

(Received May 8, 2020)

ABSTRACT

Monte Carlo numerical solutions to the radiation transfer equation in curved spacetime require both sampling of radiation-matter interactions and calculation of the null geodesics for photon trajectories. Our code, written in `C++` using the Athena++ grid framework, integrates geodesics in general spacetimes, with a particular focus on Kerr metric of spinning black holes. Since our main intent is studying accretion disks around supermassive black holes, we include free-free absorption and emission along with polarized or unpolarized Compton scattering. After showing convergence and performance comparisons to other codes on test problems, we generate synthetic spectra from accretion disk models and simulations.

Keywords: accretion, accretion disks – black hole physics – methods: numerical – radiative transfer – relativistic processes

1. INTRODUCTION

It is currently agreed that quasars and active galactic nuclei (AGN) must be accreting supermassive black holes (SMBH) due to their high luminosities and small spatial scales. While the physical processes governing their behavior are well understood, solving these interdependent, non-linear, multivariable equations nearly necessitates either unrealistic assumptions or numerical methods. AGN have become a hot topic in recent literature because of the growing tensions between accretion disk theory and observations (See Davis & Tchekhovskoy 2020, in press, for a recent review) and the Event Horizon Telescope Collaboration's first image of the supermassive black hole in M87 (Akiyama et al. 2019a) and expected image of Sgr A* in the near future. Modeling these objects requires Monte Carlo radiative transfer methods (MCRT), and Akiyama et al. (2019b) show how successfully these simulations can infer physical properties from observations. It is integral to continue bridging the disparities between observation and theory, and one essential avenue is creating realistic synthetic images based on numerical simulations.

Within the past 20 years, numerous general relativistic magnetohydrodynamic methods (GRMHD) using MCRT have emerged, each with their own set intended problems (Gammie et al. 2003; Li et al. 2005; Dolence et al. 2009; Schnittman & Krolik 2013; Ryan et al. 2015). These codes each have their advantages for their own applications and include complex processes such as Compton scattering and synchrotron radiation. Beyond capturing these physical mechanisms, simulations need to integrate the photon geodesics, either quasi-analytically (e.g., Dexter & Agol 2009) or numerically (e.g., Dolence et al. 2009), to an observer at infinity to generate mock images and spectra. These methods have significantly improved our understanding of the interplay between AGN jets and the black hole proprieties, but they lack flexibility to other astrophysical objects beyond neutron stars, core-collapse supernovae and X-ray binaries.

We present a general relativistic MCRT code written in `C++` based on the Athena++ grid framework (Stone et al., in press). The MCRT branch is relatively self-contained as it only relies on Athena's grid framework, but it has access to Athena's MHD solvers allowing for complex modeling within one code (Davis et al., in

Corresponding author: Eric Rohr
ecr7zs@virginia.edu

prep.). This code with the implementation of the general relativistic photon integrator can be used for a large number of astrophysical problems, and we focus on applications for AGN in the Kerr metric of a spinning black hole. We numerically integrate photon geodesics using the Verlet algorithm (Verlet 1976) and transform between reference frames using a tetrad basis formulation based on the fluid and magnetic field four-vectors with Gram-Schmidt orthogonalization. We include free-free absorption and emission in addition to unpolarized and polarized Compton scattering based on our MCRT algorithms.

The goal of this paper is to outline generally how the code runs, provide test problems and comparisons to other simulations and show example applications. § 2 outlines the methods used, including an introduction to MCRT in curved spacetime (§ 2.1), an explanation of how photon initialization (§ 2.2), the definitions of the tetrad formalism (§ 2.3) and the implementation of the covariant integrator for the photon four-wave-vector (§ 2.4); § 3 details three example problems, namely a test of numerical artifacts related to the Verlet algorithm, the orthonormal tetrad formulation using a relativistic Cartesian box and the null geodesic integrator by comparing trajectories around a spinning black hole to `geokerr` (Dexter & Agol 2009); § 4 gives an example application problem for ray-traycing photons to an observer at infinity for synethic images; and § 5 summarizes the results.

2. METHODS

2.1. *Monte Carlo Radiation Transfer*

Solving the relativistic radiation transfer equation for complex astrophysical models requires numerical methods and algorithms (Whitney 2011). There must be a way for generating photon packets or "superphotons," propagating photons along their trajectories, modeling matter-radiation interactions such as scattering, absorption and collecting outputs of escaped photons. Photon emission can be from a point source, distributed or from the boundaries. For example, an accretion disk can thermally emit photons based on a probability distribution function, or a star can be the only source of emission. MCRT relies on pseudo-random numbers to simulate superphoton lives from emission to absorption or escape, where each photon must draw some optical depth τ to move before getting absorbed or scattered. In Minkowski spacetime, superphotons travel in straight lines, so they can be "pushed" to their final position analytically. Then based on the appropriate schemes, such as free-free absorption or Compton scattering, the photons' characteristics evolve and a new optical depth is drawn. This process repeats until either the superphoton is entirely absorbed or some stopping criterion is met, such as exiting the simulation domain. Lastly the relevant outputs are collected and the next process can begin. By repeating this method for a large number of photons all undergoing these pseudo-random walks, we hope to gain physical insights into these astrophysical objects.

However curved spacetime presents additional challenges for MCRT methods. First, photon trajectories are now non-trivial and require solving the null geodesic equation either analytically or numerically. Further, absorption and scattering processes occur in the photons' rest frame, so there must be a system for transforming between the comoving (Lagrangian, fluid) and coordinate (Eulerian, static) frames. These complications greatly increase the computational resources required for the simulation, but various algorithms have been developed to facilitate modeling these systems (e.g., Li et al. 2005; Dolence et al. 2009; Schnittman & Krolik 2013). Our code boasts the advantages of being well interfaced with the Athena++ grid framework, so it is applicable to a wide range of astrophysical problems ranging from accretion disks of high spin supermassive black holes to protoplanetary disks to supernova explosions.

2.2. *Photon Initialization*

Before integration, each photon must have an initial position x^α, zone indices $i_\alpha = (i_1 i_2, i_3)$ for the right-handed triad coordinate system, direction in the local frame $k^{(a)}$, a weight w, absorption coefficient $\alpha_{\rm abs}$, scattering coefficient $\alpha_{\rm scat}$ and status flag. These requirements are independent of the emission mechanism and can be defined manually.

The position and zone indices are closely linked, and essentially choosing one set defines the other. There are certain cases where choosing the position and matching the proper indices is preferred, and vice versa. For creating an observer grid at a specific inclination angle at infinity to create synthetic images (see § 4) one needs to choose the initial position of the photon. Alternatively, if the emission depends on the MHD properties of the cell, then it is better to choose the cell and ascribe a position within said cell. In general, the initial position $x^\alpha = (x^t, \mathbf{x})$ must lie within the simulation domain $x_{1,2,3;\rm min} < x_1 < x_{1,2,3;\rm max}$[1]. For zone indices $0 < i_{1,2,3} < i_{1,2,3;\rm max}$, one can choose x^α, typically

[1] The code requires that the photon does not lie on exactly on a cell boundary. This is built-in for randomly assigning a position given the cell indices, and manual definition of the position should be careful to offset the position from any known boundary by some small ε.

with $x^t = 1$, and assign the appropriate zone indices. Alternatively, one can choose the zone indices and attribute some position within this cell. This process is independent for the choice of simulation coordinate system, though the algorithms for calculating the indices given the coordinates may vary.

The photon's direction $k^{(a)}$ is initialized in the locally flat frame and then transformed to the coordinate frame at the start of propagation (see § 2.3). The temporal component $k^{(t)}$ is directly related to the energy of the photon, and the eventual changing of its value (in the coordinate frame) describes the gravitational redshift the photon experiences during integration. The weight w is conceptually the number of photons within a given "superphoton" or photon packet and is invariant under frame transformations. This is typically set based on the emissivity of the cell or set to unity. The absorption $\alpha_{\rm abs}$ and scattering $\alpha_{\rm scat}$ coefficients determine how quickly the optical depth τ decreases to 0. There are various processes available, such as Thomson, Compton, none or user-defined functions. The status flag – EVOLVING, DESTROYED, ESCAPED – describes the current state of the photon before and after an integration step. EVOLVING tells the code to continue integration as normal, and ESCAPED means that the photon has left the simulation domain and tabulate the output. DESTROYED is more ambiguous, but it stops integration and discards the output. The flag can be set to DESTROYED if the photons gets absorbed, enters the black hole event horizon or any other user-enrolled status condition.

2.3. *Orthonormal Tetrad Formulation and Frame Transformations*

Once the photon properties are set, we need to transfer it to the coordinate frame for integration using an orthonormal tetrad basis $e^{\alpha}_{(a)}$. We couple the tetrad to the fluid four-velocity u^{α} and possibly to the magnetic field b^{α} by creating a trial basis $\tilde{e}^{\alpha}_{(a)}$

$$\tilde{e}^{\alpha}_{(0)} = u^{\alpha} \tag{1a}$$

$$\tilde{e}^{\alpha}_{(1)} = b^{\alpha} \text{ or } (0,1,0,0) \tag{1b}$$

$$\tilde{e}^{\alpha}_{(2)} = (0,0,1,0) \tag{1c}$$

$$\tilde{e}^{\alpha}_{(3)} = (0,0,0,1) \tag{1d}$$

We attempt to couple the basis to the magnetic field, but if $b^{\alpha} = 0$ then we default to a vector parallel to index-1. We employ a Gram-Schmidt orthogonalization scheme to sure that $e^{\alpha}_{(a)} e^{(a)}_{\alpha} = 0$. First, we normalize $\tilde{e}^{\alpha}_{(0)}$

$$\mathrm{NORM}\left[\tilde{e}^{\alpha}_{(0)}\right] \equiv \frac{\tilde{e}^{\alpha}_{(0)}}{\sqrt{|u^{\alpha} g_{\alpha\beta} u_{\beta}|}} \tag{2}$$

Here $g_{\alpha\beta}$ is the covariant metric that raises and lowers the fluid velocity: $u_{\alpha} = g_{\alpha\beta} u^{\beta}, u^{\alpha} = g^{\alpha\beta} u_{\beta}$. Then we project $e^{\alpha}_{(0)}$ onto $\tilde{e}^{\alpha}_{(1)}$ and subtract:

$$\mathrm{PROJS}_{e^{\alpha}_{(0)}}\left(\tilde{e}^{\alpha}_{(1)}\right) \equiv \tilde{e}^{\alpha}_{(1)} - e^{\alpha}_{(0)} \left(\frac{\tilde{e}^{\alpha}_{(1)} g_{\alpha\beta} e^{\alpha}_{(0)}}{e^{\alpha}_{(0)} g_{\alpha\beta} e^{\alpha}_{(0)}}\right) \tag{3}$$

Then we normalize and repeat the process for the remaining basis four-vectors

$$e^{\alpha}_{(0)} = \mathrm{NORM}\left[\tilde{e}^{\alpha}_{(0)}\right] \tag{4a}$$

$$e^{\alpha}_{(1)} = \mathrm{NORM}\left[\mathrm{PROJS}_{e^{\alpha}_{(0)}}\left(\tilde{e}^{\alpha}_{(1)}\right)\right] \tag{4b}$$

$$e^{\alpha}_{(2)} = \mathrm{NORM}\left[\mathrm{PROJS}_{e^{\alpha}_{(1)}}\left(\mathrm{PROJS}_{e^{\alpha}_{(0)}}(\tilde{e}^{\alpha}_{(2)})\right)\right] \tag{4c}$$

$$\begin{aligned} e^{\alpha}_{(3)} = \mathrm{NORM}\Big[& \\ & \mathrm{PROJS}_{e^{\alpha}_{(2)}}\left(\mathrm{PROJS}_{e^{\alpha}_{(1)}}(\mathrm{PROJS}_{e^{\alpha}_{(0)}}(\tilde{e}^{\alpha}_{(2)}))\right)\Big] \end{aligned} \tag{4d}$$

This completes the orthonormal tetrad basis. The photon direction can now be transformed between frames using

$$k^{\alpha} = e^{\alpha}_{(a)} k^{(a)} \tag{5a}$$

$$k^{(a)} = e^{(a)}_{\alpha} k^{\alpha} \tag{5b}$$

where $e^{(a)}_{\alpha} = g_{\alpha\beta} e^{\alpha}_{(a)}$. Additionally, $\nu\alpha$ is a conserved quantity, where ν and $\alpha = \alpha_{\rm abs} + \alpha_{\rm scat}$ are the photon's frequency and opacity respectively. The frequency is related to the time-like component of the photon's direction

$$\nu_{\rm tet} = -e^{\alpha}_{(0)} k_{\alpha} = -u^{\alpha} k_{\alpha} \tag{6a}$$

$$\nu_{\rm coord} = -k^{\alpha} g_{\alpha\beta} u^{\beta} = k_t \tag{6b}$$

Then the opacities can be transformed using the the photon's direction and and fluid four-velocity

$$\alpha_{\rm tet} = \left(\frac{\nu_{\rm tet}}{\nu_{\rm coord}}\right) \alpha_{\rm coord} = -\left(\frac{k^t}{k^{\alpha} u^{\beta}}\right) \alpha_{\rm coord} \tag{7a}$$

$$\alpha_{\rm coord} = \left(\frac{\nu_{\rm coord}}{\nu_{\rm tet}}\right) \alpha_{\rm tet} = -\frac{k^{\alpha} g_{\alpha\beta} u^{\beta}}{k^t} \alpha_{\rm tet} \tag{7b}$$

2.4. *Covariant Integrator*

Unlike in Minkowski spacetime where photons can be analytically pushed until hitting a boundary or reaching an optical depth of 0, radiation transfer in arbitrary spacetimes require integration of the geodesic equation. First, the photon's direction k^α is defined by

$$k^\alpha \equiv \frac{dx^\alpha}{d\lambda} \tag{8}$$

where λ is the affine parameter. Then the geodesic equation governing the changing photon direction and energy is

$$\frac{dk^\alpha}{d\lambda} = -\Gamma^\alpha_{\beta\gamma} k^\beta k^\gamma \tag{9}$$

where $\Gamma^\alpha_{\beta\gamma}$ are the connection coefficients defined by

$$\Gamma^\alpha_{\beta\gamma} \equiv \frac{1}{2} g^{\alpha\delta} \left(g_{\delta\beta,\gamma} + g_{\delta\gamma,\beta} - g_{\beta\gamma,\delta} \right) \tag{10}$$

for arbitrary metrics and and any coordinate basis. There are four constants of motion, listed in Kerr-Schild coordinates (t, r, θ, ϕ): the energy at infinity $E = k_t$; the angular momentum $l = k_\phi$; Carter's constant $Q = k_\theta^2 + k_\phi^2 \cot^2\theta - a^2 k_t^2 \cos^2\theta$ where a is the dimensionless black hole spin parameter; and the photon trajectory must be time-like $k^\alpha k_\beta = 0$ (Carter 1968). These constraints can be used to solve differential equations Eqs. (9), (10) analytically to obtain x^α and k^α based on the initial or final position and wave vector, as is done in `geokerr` (Dexter & Agol 2009).

However, we choose an ordinary differential equation algorithm rather than directly integrating the the equations of motion. We use the velocity Verlet algorithm because it requires only one evaluation of the connection coefficients $\Gamma^\alpha_{\beta\gamma}$ per step $\Delta\lambda$, and Dolence et al. (2009) showed that this method is faster than higher order integration schemes in `grmonty`. For the geodesic equation Eq. (9), the Verlet algorithm for iteration $n+1$ is

$$x^\alpha_{n+1} = x^\alpha_n + k^\alpha_n \Delta\lambda + \frac{1}{2}\left(\frac{dk^\alpha}{d\lambda}\right)_n (\Delta\lambda)^2 \tag{11a}$$

$$k^\alpha_{n+1,p} = k^\alpha_n + \left(\frac{dk^\alpha}{d\lambda}\right)_n (\Delta\lambda) \tag{11b}$$

$$\left(\frac{dk^\alpha}{d\lambda}\right)_{n+1} = -\Gamma^\alpha_{\beta\gamma} k^\beta_{n+1,p} k^\gamma_{n+1,p} \tag{11c}$$

$$k^\alpha_{n+1} = k^\alpha_n + \frac{1}{2}\left[\left(\frac{dk^\alpha}{d\lambda}\right)_n + \left(\frac{dk^\alpha}{d\lambda}\right)_{n+1}\right](\Delta\lambda) \tag{11d}$$

where $\Gamma^\alpha_{\beta\gamma} = \Gamma^\alpha_{\beta\gamma}(\mathbf{x}_{n+1})$ are the connection coefficients evaluated at the position three-vector $\mathbf{x}_{n+1}$ of iteration $n+1$. Eq. (11) is repeated until the error is less than some tolerance $\mathcal{E} \sim 10^{-3} - 10^{-5}$:

$$\mathcal{E} < \frac{\left|k^\alpha_{n+1} - k^\alpha_n\right|}{k^\alpha_n} \tag{12}$$

or if the maximum number of iterations is reached (very rarely and then the photon is destroyed). This typically requires < 10 iterations for our conservative tolerance chosen $\mathcal{E} = 10^{-5}$. The photon's energy E_{n+1} is also updated at each step

$$E_{n+1} = E_n \left(\frac{k^t_{n+1}}{k^t_n}\right) \tag{13}$$

after k^α_{n+1} has converged.

The stepsize is parameterized by a fractional value ϵ relating the physical size of the grid cell and the photon's wave vector. In grid cell i the stepsize is defined by

$$\Delta\lambda = \mathrm{MIN}\left[\frac{\mathrm{MAX}(\alpha_i) - \mathrm{MIN}(\alpha_i)}{k^\alpha}\right]\epsilon \tag{14}$$

where $\alpha = x^1, x^2, x^3$ are the right-hand triad for spatial coordinates.

3. COMPARISONS AND PERFORMANCE TESTS

We create and run test problems to ensure the accuracy of the various parts – stepsize effects, orthonormal tetrad formulation, Verlet integration of the geodesic equation – of the photon propagation.

First, we test the affect of the stepsize parameter on the photon propagation. We emit 10^3 photons uniformly and isotropically in a spherical-polar domain of radius $R = 100 r_0$ in arbitrary units. Then we vary the stepsize parameter in units of r_0 and integrate the photons until they exit the simulation domain. We compute the difference between the numerical and analytic solution's exit positions and divide by the simulation domain size R. Figure 1 graphs the median of this fractional error versus ϵ, and the results follow a linear relationship. We consider stepsizes $\epsilon \lesssim 10^{-2}$, with median error $\Delta r/R \sim 10^{-3}$, to be sufficiently accurate while maintaining efficiency; we choose $\epsilon = 10^{-2}$ for the remainder of this paper unless otherwise stated. However, for very large simulation domains that use logarithmic spacing, we recommend smaller stepsizes $\epsilon \lesssim 10^{-3}$ to ensure the accuracy of geodesic integration.

Second, we test the frame transformations using a moving Cartesian box and coordinate basis (t, x, y, z). We emit 10^5 photons from free-free emission uniformly from gas of temperature $T = 10^5$ [K] within a large box of size $R = 10^{13} r_0$ in arbitrary units in each direction. We then attribute some velocity $\beta = v/c$ that the box

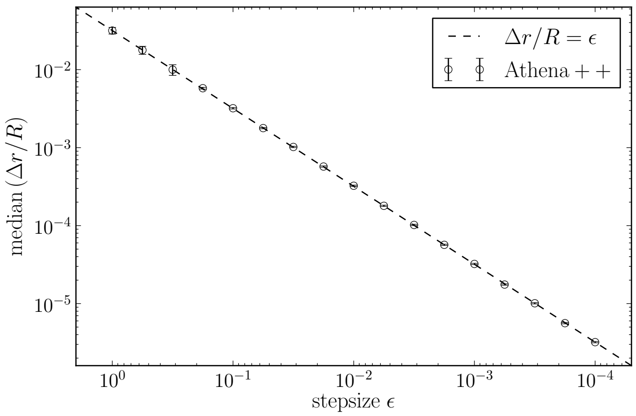

Figure 1. 1000 photons integrated at each step size in flat spacetime in spherical-polar coordinates, starting at 10^0 and ending at 10^{-4} in steps of $10^{-1/4}$. The mean fractional error between analytic and integrated exit position decreases linearly with stepsize parameter. We consider stepsizes $\sim 10^{-2} - 10^{-3}$ to be sufficiently accurate while maintaining speed.

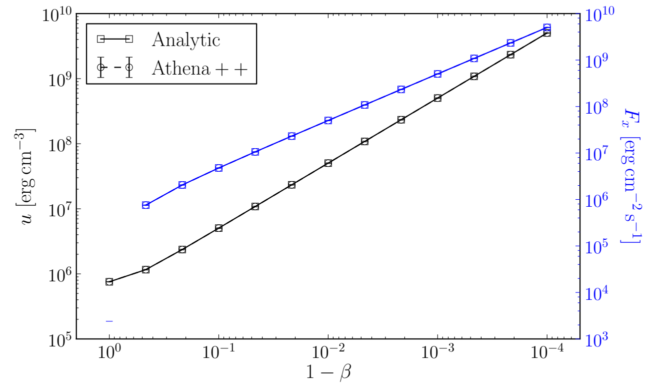

Figure 2. 10^5 photons emitted isotropically and propagated until absorption in a periodic Cartesian box, which moves in the positive x direction at some velocity $\beta = v/c$. The black curves and left vertical axis are the energy density u, while the blue curves and right vertical axis are the flux F_x in the $\hat{\mathbf{x}}$ direction. The analytic and integrated results agree to $< 1\sigma$, typically $\lesssim 10^{-2} - 10^{-3}\sigma$, for all velocities and stepsizes $\epsilon \lesssim 10^{-2}$.

moves in the positive $\hat{\mathbf{x}}$ direction. After initializing the photons in their local rest frame we transform to the coordinate frame using

$$\tilde{e}^{\alpha}_{(t)} = u^{\alpha} = (\gamma, \gamma\beta, 0, 0) \tag{15}$$

as the time-like four-vector of orthonormal tetrad where γ is the Lorentz factor. Then we propagate the photons until they are free-free absorbed (i.e., until they have traveled one randomly drawn optical depth τ) and then are transformed back into the local rest frame. We sum the energy density and flux of the absorbed photons, and figure 2 summarizes the results, with the black and blue curves referring to the energy density and flux respectively. For flat spacetime and a relativistic box, the energy density u and flux F_x follow analytic expressions (open squares):

$$u = aT^4\gamma^2\left(1 + \frac{1}{3}\beta^2\right) \tag{16}$$

$$F_x = \frac{4}{3}\gamma^2 aT^4\beta \tag{17}$$

where a is the radiation constant (Mihalas & Mihalas 1984). For all velocities tested and a stepsize parameter $\epsilon = 10^{-2}$, the analytic and numerical calculations agree to $< 1\sigma$ affirming a proper orthonormal tetrad formulation.

Lastly, we test the accuracy of the geodesic equation integration via Verlet algorithm by propagating photons near a high spin black hole. We emit 32 photons isotropically in the rest frame at the radius of the innermost stable circular orbit $r_{\rm isco}$ of a black hole of spin $a/M = 0.9375$ at the equatorial plane (black dots):

$$x^{\alpha} = (1, r_{\rm isco}, \pi/2, 0) \tag{18}$$

We transform into the comoving frame using ring emission for the fluid velocity

$$u^{\alpha} = u^t\,(1, 0, 0, \Omega)\,, \qquad \Omega = \frac{1}{r^{3/2} + a} \tag{19}$$

in Kerr-Schild coordinates where Ω is the prograde orbital velocity. The normalization condition in characteristic units of $R_g = GM/c^2 = 1$ yields

$$u^{\alpha} g_{\alpha\beta} u^{\beta} = \left(u^t\right)^2 g_{tt} + 2\left(u^t\right)^2 g_{\phi t}\Omega + \left(u^t\right)^2\Omega^2 g_{\phi\phi} = -1$$
$$\Rightarrow u^t = \pm\left[\frac{-1}{g_{tt} + 2g_{t\phi} + \Omega^2 g_{\phi\phi}}\right]^{1/2} \tag{20}$$

and we choose the positive root. We integrate the geodesic equation until the photon enters the event horizon $r_{\rm EH} = 1 + \sqrt{1 - a^2}$ or reaches an outer radius $R = 100R_g$, and Figure 3 plots the trajectories (black circles). Dexter & Agol (2009)'s `geokerr`'s quasi-analytic solution are overplotted (red lines) and the two trajectories agree well, confirming the accuracy of our geodesic integration.

4. APPLICATION PROBLEMS

One useful application of the general relativistic photon integrator is creating synthetic observations of accreting black holes. We create a grid of impact parameters to initialize photons at a large radius $r_0 \gg r_g = 1$

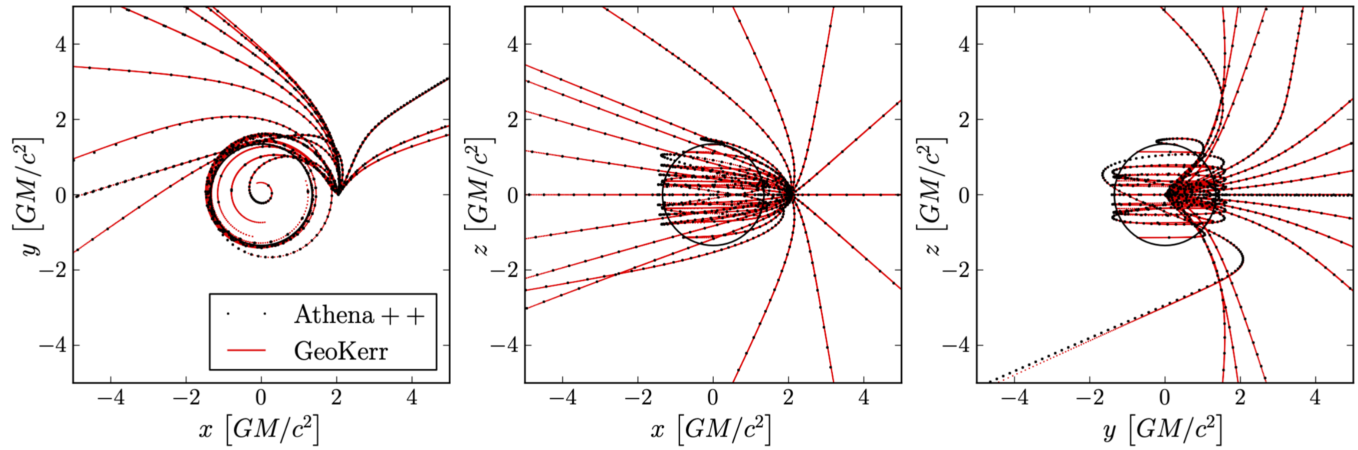

Figure 3. 32 photons emitted isotropically in the fluid frame from $R_{\rm isco} \sim 2.04\,R_g$ for spin $a/M = 0.9375$ (compare with Dolence et al. (2009)'s Figure 1). The stepsize parameter is 10^{-2}, and `geokerr`'s resolution is 700 points per geodesic. The Athena++ circles are plotted every 200 steps, and the integration is carried out to 100 R_g.

and ray-trace back to the black hole and accretion disk. In the photon rest frame these parameters are defined by Cunningham (1973) as

$$\alpha = \lim_{r_0\to\infty} -r_0 \frac{k^{(\phi)}}{k^{(t)}} \tag{21}$$

$$\beta = \lim_{r_0\to\infty} r_0 \frac{k^{(\theta)}}{k^{(t)}} \tag{22}$$

Using these definitions in units of $k^{(t)}$ and the null geodesic condition allow for k^α to be set solely by choosing a pair (α, β) (Agol 1997; Dexter & Agol 2009). The light-like wave-vector yields a quadratic equation for k_r in the coordinate frame

$$\begin{aligned}
&(k_r)^2\,\gamma + k_r\zeta + \xi = 0,\\
&\gamma = g^{rr}\\
&\zeta = k_t\left(g^{rt} + g^{r\theta}\beta - g^{r\phi}\alpha\right)\\
&\xi = (k_t)^2 \times\\
&\quad\left(g^{tt} + 2g^{t\theta}\beta - 2g^{t\phi}\alpha + g^{\theta\theta}\beta^2 + g^{\phi\phi}\alpha^2 - 2g^{\theta\phi}\alpha\beta\right)
\end{aligned} \tag{23}$$

in Kerr-Schild coordinates. Consequently, choosing (α, β) uniquely determines k_α

$$k_t = 1 \tag{24a}$$

$$k_r = \frac{-\zeta \pm \sqrt{\zeta^2 - 4\gamma\xi}}{2\gamma} \tag{24b}$$

$$k_\theta = \beta k_t \tag{24c}$$

$$k_\phi = -\alpha k_t \tag{24d}$$

and we choose the root such that $k_r < 0$ for Eq. (24b) so the photon travels towards the region of interest. Then we raise the wave vector and divide each component by k^t such that the initial time-like component is $k^t = 1$, allowing for easy tracking of gravitational redshift and beaming/lensing effects.

Because the wave-vector is initialized in the coordinate frame already, we can skip transforming between frames and begin integrating the geodesic equation. We set the initial position

$$x^\alpha = (1, r_0, \theta, 0) \tag{25}$$

for colatitutde $\theta \in (0, \pi/2)$ that can be varied for different viewing inclination angles. We require $r_0 \gg r_g$ and $r_0 \gg r_{\rm disk}$, the outer radius of the accretion disk defining the region of interest. Then we integrate the geodesic equation until the photon

- reaches the black hole event horizon $x^r \leq r_{\rm EH}$,
- reaches the equatorial plane $x^\theta \geq \pi/2$ at $x^r \leq R_{\rm disk}$
- or exits the simulation domain $x^r \geq R$

If the photon meets the second condition, it is transformed into tetrad frame using the standard ring emission fluid velocity Eq. (19), (20) to calculate the photon's redshift $z = k^{(t)}$ (since $k^t_{\rm em} = 1$). Figure 4 displays nine example images, showing three inclination angles $\mu = \cos\theta$ for three different spin SMBHs. For these images, the integration begins at $r_0 = 10^4 r_g$, has a disk radius $R_{\rm disk} = 100 r_g$, stepsize $\epsilon = 10^{-3}$, and $\alpha < 0$ corresponds to the fluid coming towards the observer. Similarly, Figure 5 has the same parameters as Figure 4-3a, except the outer disk radius is $R_{\rm disk} = 15 r_g$ to show the black hole shadow.

If the photon exits the simulation grid or if it's final position is within $x^r < r_{\rm isco}$, then we attribute zero in-

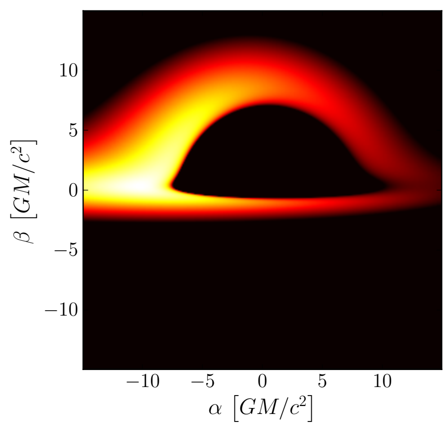

(1a) $a = 0,\ \mu = 0.1$

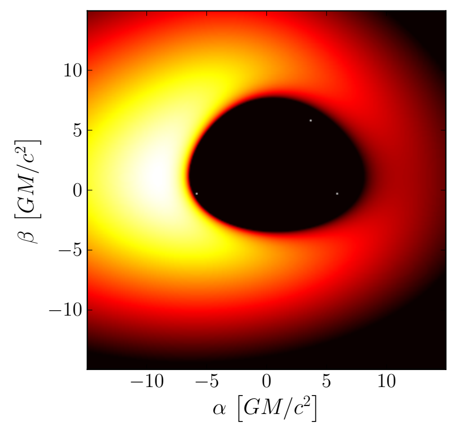

(1b) $a = 0,\ \mu = 0.5$

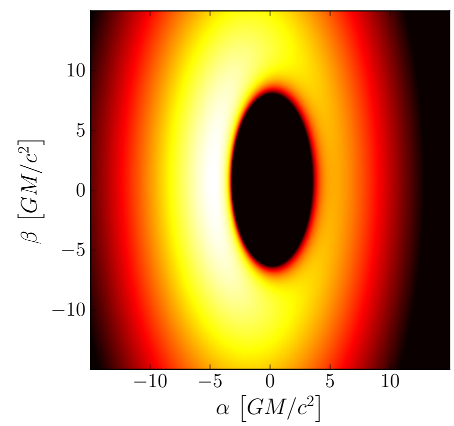

(1c) $a = 0, \mu = 0.9$

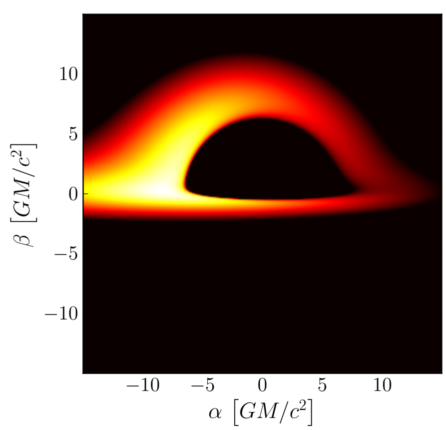

(2a) $a = 0.45,\ \mu = 0.1$

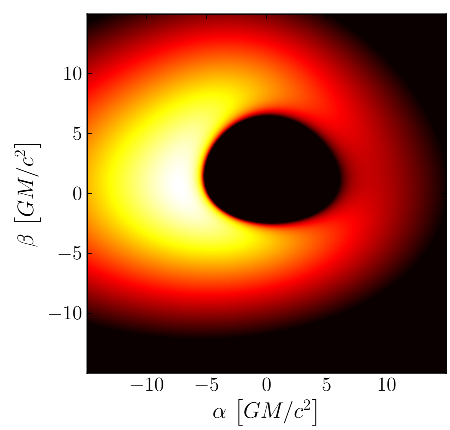

(2b) $a = 0.45,\ \mu = 0.5$

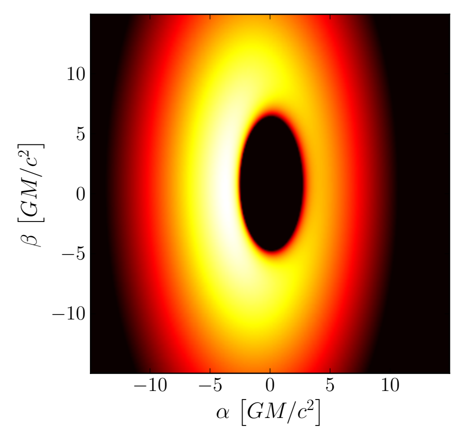

(2c) $a = 0.45,\ \mu = 0.9$

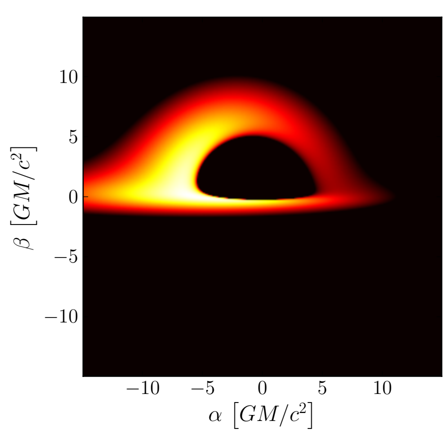

(3a) $a = 0.9,\ \mu = 0.1$

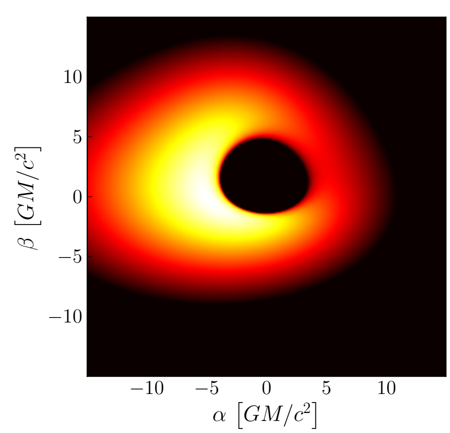

(3b) $a = 0.9,\ \mu = 0.5$

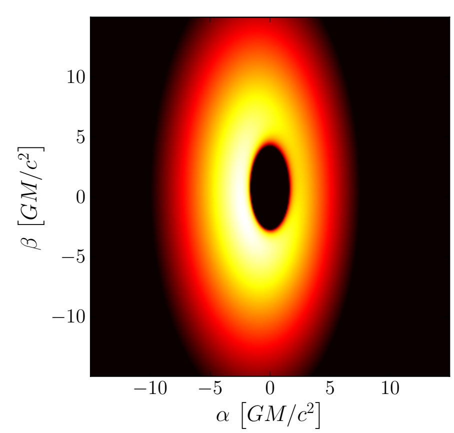

(3c) $a = 0.9,\ \mu = 0.9$

Figure 4. Nine images of supermassive black holes $M = 10^9\,\mathrm{M}_\odot$ with three spins $a = 0.0, 0.45, 0.9$ viewed from three inclination angles $\mu = 0.1, 0.5, 0.9$. The photons are traced back from a large distance $r_0 = 10^4 r_g$ back to the black hole disk in a logarithmic grid and stepsize $\epsilon = 10^{-3}$, where there are transformed into the fluid frame and emit thermally. These images assume an observed photon frequency $\nu_{\rm obs} = 5 \times 10^{15}$ Hz, black hole mass $M_{\rm BH} = 10^9\,\mathrm{M}_\odot$ an accretion ratio of $\dot{M}/\dot{M}_{\rm Edd} = 0.1$, and there are 90000 photons emitted uniformly in (α, β) pairs from $\alpha, \beta \in (-15, 15)$. Effects from relativistic beaming, frame dragging and light bending are present.

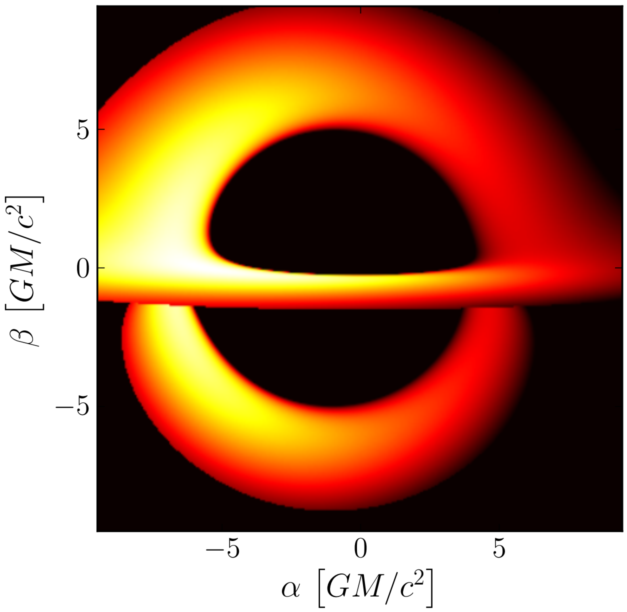

Figure 5. The same black hole as Figure 4-3a, except with an outer disk radius $R_{\rm disk} = 15r_g$ to show the black hole shadow, and the 102400 photons are uniformly emitted in (α, β) pairs from $\alpha, \beta \in (-10, 10)$.

tensity to this (α, β). For all other photons that reach the equatorial plane at $r_{\rm isco} < r < R_{\rm disk}$ we attribute the general relativistic correction to the blackbody intensity. We use the standard blackbody flux $f_{\rm BB}(r)$ to calculate the temperature

$$T_{\rm BB} = \left(\frac{f_{\rm BB}(r)}{\sigma}\right)^{1/4} \tag{26}$$

where σ is the Stefan-Boltzmann constant. Then we find the effective temperature $T_{\rm eff}$ using Novikov (1973)'s general relativistic temperature correction $T_{\rm corr}$ such that $T_{\rm eff} = T_{\rm BB} \times T_{\rm corr}$. Using the observed frequency $\nu_{\rm obs}$ and the redshift z to determine the emitted frequency $\nu_{\rm obs} = z\nu_{\rm em}$, we calculate the emitted intensity $I_{\rm em} = \nu B_\nu(T_{\rm eff}, \nu_{\rm em})$. Finally, we convert the intensity from emitted to observed via

$$I_{\rm obs} = I_{\rm em}\left(\frac{\nu_{\rm obs}}{\nu_{\rm em}}\right)^3 \tag{27}$$

Figure 4 assumes an observed photon frequency $\nu_{\rm obs} = 5 \times 10^{15}$ Hz, black hole mass $M_{\rm BH} = 10^9\,{\rm M}_\odot$ and an accretion ratio of $\dot{M}/\dot{M}_{\rm Edd} = 0.1$. Figure 4 emits 90000 photons uniformly in (α, β) pairs from $\alpha, \beta \in (-15, 15)$, while Figure 5 emits 102400 photons uniformly in (α, β) pairs from $\alpha, \beta \in (-10, 10)$. The effects from relativistic beaming, frame dragging and light bending are all present and naturally accounted for via the frame transformations and geodesic integration.

5. SUMMARY

We have presented a fully general relativistic Monte Carlo radiative transfer branch of the magnetohydrodynamic grid-based Athena++. We emphasize that this code and the entirety of the Athena++ domain have wide astrophysical applications, but we focus our attention on bridging the gaps between supermassive black hole accretion theory and observations. After outlining the difficulties of solving the relativist radiative transfer equation in curved spacetime, we explain the code's methods for creating superphotons within the Athena++ grid framework. The code utilizes an orthonormal tetrad formulation based on the Gram-Schmidt orthogonalization technique and fluid & potentially magnetic field four-vectors to transform between the fluid and static frames. Upon completion of the photon initialization, we employ the velocity Verlet algorithm to solve the null geodesic equation while continuously updating the photon's properties until termination or some matter-radiation interaction occurs.

After this detailed explanation of the code's methods, we confirm it's accuracy and speed via comparisons to analytic expressions and other works. We test the accuracy of the Verlet algorithm's stepsize parameter ϵ by integrating geodesics in spherical-polar coordinates in Minkowski spacetime, where Figure 1 shows that choosing $\epsilon \lesssim 10^{-1}$ preserves accuracy while maintaining competitive speed. Figure 2 affirms the accuracy of the tetrad formulation by calculating the energy density u and flux F_x of a relativistic Cartesian box and comparing against expressions from Mihalas & Mihalas (1984). The final problem tests the accuracy of the geodesic integration by comparing the trajectories of 32 photons emitted isotropically in the fluid frame at the innermost stable circular orbit of a spinning black hole to `geokerr`'s quasi-analytic solutions (Dexter & Agol 2009), and Figure 3 displays our code's accuracy.

Finally, we detail an example application problem of generating synthetic images by creating an observer grid at infinity and ray-tracing photons back to the black hole and accretion disk. Figure 4 beautifully boasts two such photometric images of high spin black holes viewed nearly edge-on, where beaming, lensing and light-bending effects are all present. While not shown here, the same application can be used to create synthetic spectra of AGN.

E.R. acknowledges the help and guidance of S.D. in the creation of this code and manuscript, both in the direct help S.D. has given E.R. and in assisting the numerous previous students that have facilitated the progression of this code – namely Robin Leichtnam, Samer

El-Abd and Eli Golub. E.R. also acknowledges the financial support provided by S.D.'s NSF grant, in addition to the University of Virginia's Department of Astronomy distinguished major program degree requirements for the "encouragement" to complete the work necessary for this manuscript. Lastly, E.R. extends his deepest appreciation to StackOverflow and the `C++` documentation for answering every introductory syntactical question throughout this research period, the numerous colleagues that have continuously guided his trajectory in astrophysical research over the past four years and the existence of alcohol in making said trajectory, specifically the completion of this thesis, tolerable and enjoyable.

REFERENCES

Agol, E. 1997, PhD thesis, University of California Santa Barbara

Akiyama, K., Alberdi, A., Alef, W., et al. 2019a, The Astrophysical Journal, 875, L1

—. 2019b, The Astrophysical Journal, 875, L6

Carter, B. 1968, Physical Review, 174, 1559

Cunningham, C. T., B. J. M. 1973, ApJ, 183, 247

Dexter, J., & Agol, E. 2009, Astrophysical Journal, 696, 1616

Dolence, J. C., Gammie, C. F., Mościbrodzka, M., & Leung, P. K. 2009, Astrophysical Journal, Supplement Series, 184, 387

Gammie, C. F., McKinney, J. C., & Toth, G. 2003, The Astrophysical Journal, 589, 444

Li, L., Zimmerman, E. R., Narayan, R., & McClintock, J. E. 2005, The Astrophysical Journal Supplement Series, 157, 335

Mihalas, D., & Mihalas, B. W. 1984, Foundations of Radiation Hydrodynamics (New York: Oxford University Press), 1–731

Novikov, I.D.; Thorne, K. S. 1973, in Summer School of Theoretical Physics (Les Houches: Gordon and Breach, Science Publishes, Inc.)

Ryan, B. R., Dolence, J. C., & Gammie, C. F. 2015, Astrophysical Journal, 807, 31

Schnittman, J. D., & Krolik, J. H. 2013, Astrophysical Journal, 777, doi:10.1088/0004-637X/777/1/11

Verlet, L. 1976, Physical Review, 159, 98

Whitney, B. A. 2011, Bulletin of Astronomical Society of India, 39, 101